Proceedings World Geothermal Congress 2015
Melbourne, Australia, 19-25 April 2015

Characterization of Fracture Plane Heterogeneity Using Variogram Models

Carla Kathryn Co and Roland N. Horne

Department of Energy Resources Engineering, Stanford University, Stanford, CA 94305

carlakdc@stanford.edu

Keywords: shear fractures, variogram models, fracture heterogeneity

ABSTRACT

In geothermal reservoirs, where fractures are the main conduits for flow, the accurate modeling of flow through fractures is important in maximizing energy production. It is often assumed that the aperture is constant within the fracture. Though this is a good approximation, it does not take fracture roughness into account. Flow experiments in rough fractures have demonstrated that flow channeling can occur in fractures with heterogeneous aperture and permeability distributions. Flow channeling can impact geothermal energy production because it reduces the surface area available for heat conduction from the surrounding rock matrix. Characterization of the fracture aperture is important because aperture is directly related to permeability.

In this study, the main goal was to present a structure for the characterization of fracture aperture distribution of different rock samples and pairing configurations. Variogram models and frequency distribution plots were used to characterize the roughness of fracture planes. Geostatistical techniques were used to analyze the spatial distribution of aperture values within the fracture plane. The best fit variogram models for fracture surfaces generated with a shear offset showed higher spatial continuity in the direction perpendicular to the direction of the shear offset. In contrast, the variogram models for mated fracture surfaces created artificially with a wedge exhibited no preferential orientation. Future work will include flow simulations to correlate characterization parameters to flow channeling effects.

1. INTRODUCTION

Faults and fractures are the main conduits for flow in geothermal reservoirs. Therefore, understanding the fundamental physics of flow within fractures is important in reservoir management. Typically, the parallel plate model is assumed for numerical simulations, where a single aperture is specified for the whole fracture plane. Using the cubic law, this also implies that the fracture permeability is constant and isotropic. However, flow experiments conducted in rough fractures have consistently shown heterogeneous flow or flow channeling. Figure 1 shows significant flow channeling in numerical simulations conducted by Ishibashi et al. (2012) for two natural fractures. Moreover, flow channeling reduces the available heat transfer area for conduction. This phenomenon can have a significant impact in heat transport because most of the heat comes from the surrounding matrix rocks.

To model the flow correctly, the spatial distribution of fracture aperture must be characterized accurately. Characterization provides different parameters and methods to describe the roughness within the fracture plane. Knowledge of these parameters enables one to define the relationships between the roughness distribution and the different generation mechanisms. These parameters can likewise be correlated to the impact of fracture roughness on heat and mass transport processes. The fracture roughness distribution can be described in terms of summary statistics and spatial distributions. One way of describing the aperture variation within the fracture plane is to determine its distribution. Through these distributions, the key summary statistics can be found (Isaaks and Srivastava, 1989; Goovaerts, 1997). The more common types of distributions observed in fractures are the normal or Gaussian and lognormal distributions. For the lognormal distribution, the logarithm of the parameter is normally distributed. Several studies have shown a Gaussian distribution for the aperture (Hakami and Larsson, 1996; Pyrak-Nolte et al., 1997; Lee and Cho, 2002; Sausse, 2002). In contrast, the lognormal aperture distribution behavior has been observed in other studies (Gale, 1987; Renshaw, 1995; Watanabe et al., 2008, 2009; Ishibashi et al., 2012). The lognormal behavior is attributed to the high degree of skewness and the long tail of the histograms (Watanabe et al., 2008). Iwano and Einstein (1993) have shown both normal and lognormal distribution curves. Identifying the correct distribution function is very important when estimating extreme values (Isaaks and Srivastava, 1989).

Although summary statistics from histograms of fracture aperture values are useful, these are often not adequate. Understanding the spatial distribution of aperture values within a fracture is important in identifying the possible generation mechanisms for the roughness. Moreover, inferences from spatial relationships can be used to establish the conditions at which the impact of fracture roughness on transport processes becomes relevant. Furthermore, geostatistical techniques can be used to recreate aperture distributions that result in flow channeling. Using geostatistical techniques, two-point spatial relationships can be quantified using the semivariogram (Goovaerts, 1997). Variogram modeling for the spatial distribution of fracture aperture has been used in several studies (Iwano and Einstein, 1993; Hakami and Larsson, 1996; Lee and Cho, 2002). The fractal dimension of surfaces can also be determined by using the variogram method (Klinkenberg, 1994). In this study, the variogram will be used to quantify spatial correlations of aperture distributions in fault planes. Variogram modeling can be done automatically using the Stanford geostatistical modeling software (SGeMs) program (Remy et al., 2009).

Two main data sets, wedge fractures and shear fractures, were analyzed. Wedge fracture surfaces were generated artificially by driving a wedge through a granite rock sample (Ishibashi et al., 2012). On the other hand, shear fracture surfaces were generated in compression tests performed on sandstone and granite core samples. Wedge fracture aperture data were provided by Takuya Ishibashi while shear fracture surface elevation maps were from David Pollard, a professor at the Department of Geological and Environmental Sciences at Stanford University. For the shear fracture samples, surface elevation values were measured using a

laser scanner. Aperture maps for different fracture surface pairing configurations were generated. For the wedge fractures, aperture maps for the mated and sheared configurations were compared. Fractures with a sheared surface pairing configuration had a shear offset in the y direction while fractures with a mated surface pairing configuration had no shear offset. Similarly, mated and sheared fracture surface pairing configurations for shear fractures were compared.

The main goal of this study was to provide a framework for systematic fracture aperture characterization. Characterization parameters for the roughness of different fracture surfaces were determined. Frequency distribution curves were compared to observe the relative distribution of small and large aperture values. In addition, best fit variogram models were generated to match experimental variograms. Based on the variogram models, trends of spatial continuity were inferred. Orientations of high spatial correlation were then correlated with the generation mechanisms in terms of pairing configuration and the direction of shear.

Aside from the identification of fracture generation mechanisms, variogram parameters can be used to relate the fracture aperture characterization parameters to flow channeling. In addition, variogram models and histogram plots can be used to generate multiple realizations of fracture aperture maps that have the same texture. Fracture permeability maps can then be generated from the aperture maps by using the cubic law. The next step in this study will be to perform flow simulations to correlate the characterization parameters to flow channeling effects.

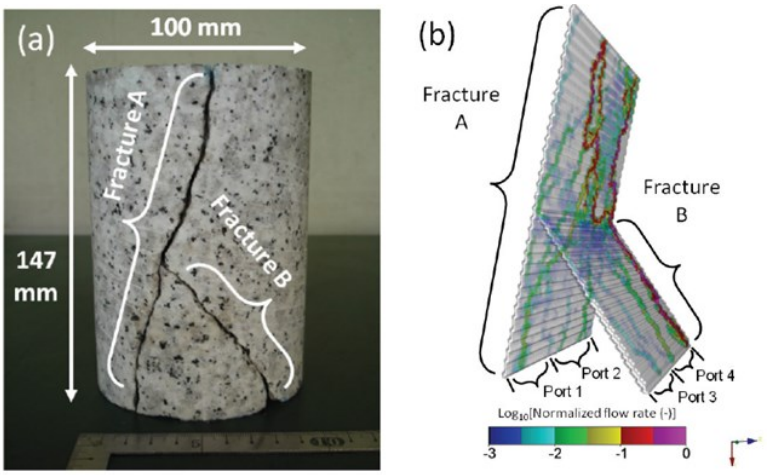

Figure 1: Experiments on flow channeling (from Ishibashi et al., 2012). Left: photograph of a granite rock sample with two intersecting fractures. Right: fluid flow simulation results showing flow channeling within rough fractures.

2. APERTURE DATA

Two fracture data sets were collected for analysis. One fracture aperture data set is from Ishibashi et al. (2012), where fracture surfaces were created using a wedge on granite samples. A total of three fractures at different length scales were generated. Then, fracture aperture maps were generated by matching the two fracture surfaces together until the flow simulation results agreed with experimental data. The second data set consisted of fracture surface elevation maps from four core samples sheared in compression tests performed by David Lockner at the United States Geological Survey (USGS) in Menlo Park, CA. Samples 34 and 47 are composed of medium grained sandstone while samples 48 and 52 are granitic rocks. The surface elevations were measured by Rebecca Strickfaden using a laser scanner with a measurement accuracy of $\pm 0.1270\ mm$. Aperture maps were generated for different values of percent contact area.

2.1 Wedge Fracture (Ishibashi et al., 2012)

2.1.1 Wedge Fracture: Mated

Mated fractures are created by pressing the two fracture surfaces together. The three samples at different length scales are designated as small, medium, and large. Fracture aperture maps and histogram plots for the small, medium, and large cases are shown in Figure 2, Figure 3, and Figure 4, respectively. For the small grid case, the aperture map does not exhibit any trends although it shows a rough surface. On the other hand, the aperture map for the medium grid case shows some lineations with higher aperture values. Compared to the medium grid case, the large grid case has a higher degree of high aperture lineations. Furthermore, the three corresponding histogram plots indicate a lognormal frequency distribution where there are more points with low aperture values.

2.1.2 Wedge Fracture: Sheared

In contrast to mated fractures, shear fractures are generated by introducing a 5 mm offset in the y direction. Figure 5 shows the aperture map and histogram plot for the sheared fracture with a small grid. Similar to the mated fracture cases, the aperture frequency distribution is lognormal. However, unlike the mated fracture cases, there are pronounced channels with high aperture values. In addition, aperture maps for the medium (Figure 6) and large (Figure 7) grid cases also exhibit channels. Moreover, the corresponding frequency distribution plots for the medium and large grid cases also demonstrate lognormal behavior.

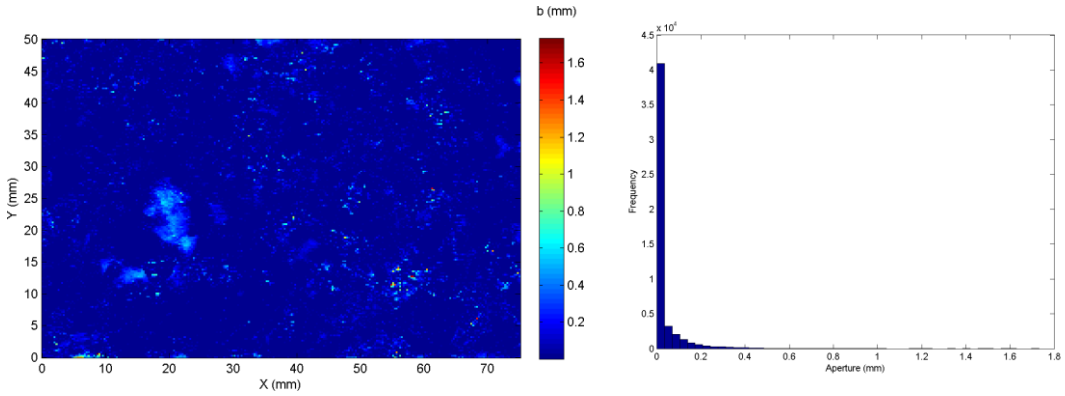

Figure 2: Fracture aperture data for the mated fracture: small grid case (75 mm x 50 mm) from Ishibashi et al. (2012). Left: aperture map. Right: histogram of the aperture distribution.

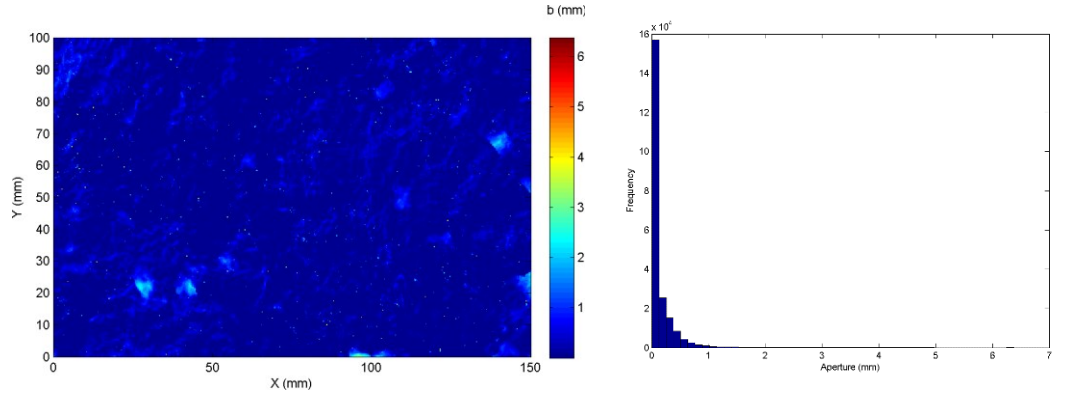

Figure 3: Fracture aperture data for the mated fracture: medium grid case (150 mm x 100 mm) from Ishibashi et al. (2012). Left: aperture map. Right: histogram of the aperture distribution.

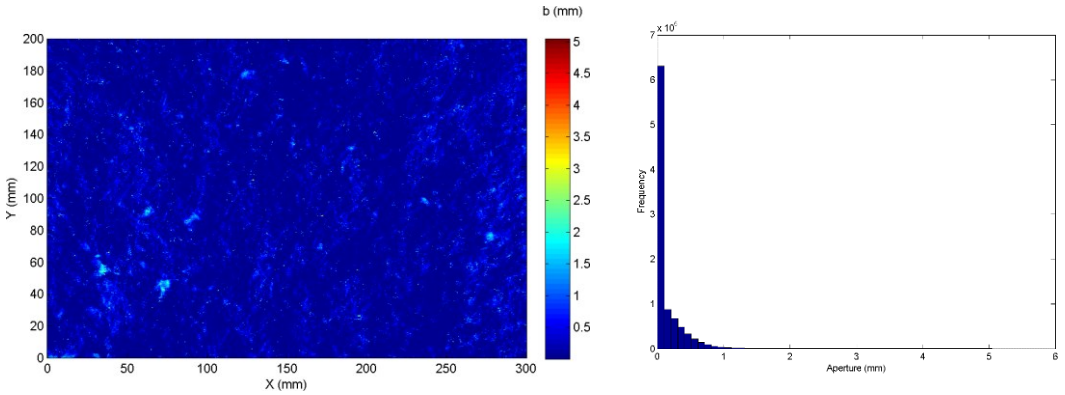

Figure 4: Fracture aperture data for the mated fracture: large grid case (300 mm x 200 mm) from Ishibashi et al. (2012). Left: aperture map. Right: histogram of the aperture distribution.

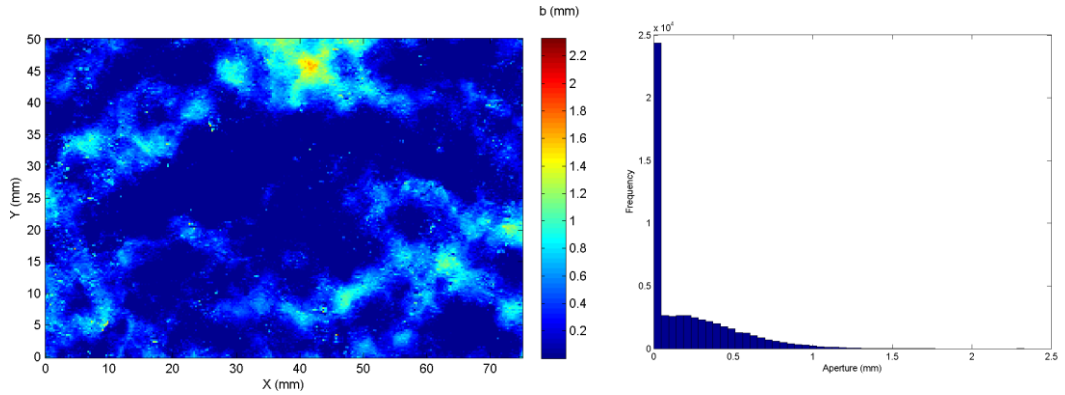

Figure 5: Fracture aperture data for the sheared fracture: small grid case from Ishibashi et al. (2012). The sample was sheared with a 5 mm offset in the y direction. Left: aperture map. Right: histogram of the aperture distribution.

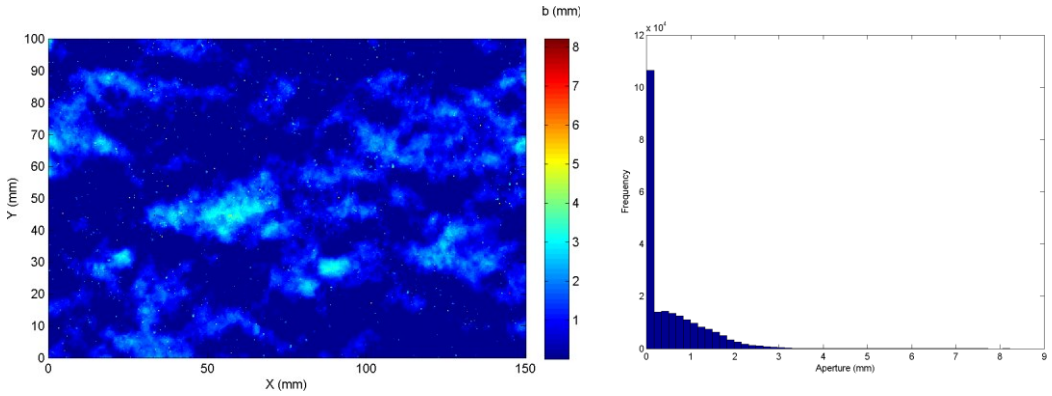

Figure 6: Fracture aperture data for the sheared fracture: medium grid case from Ishibashi et al. (2012). The sample was sheared with a 5 mm offset in the y direction. Left: aperture map. Right: histogram of the aperture distribution.

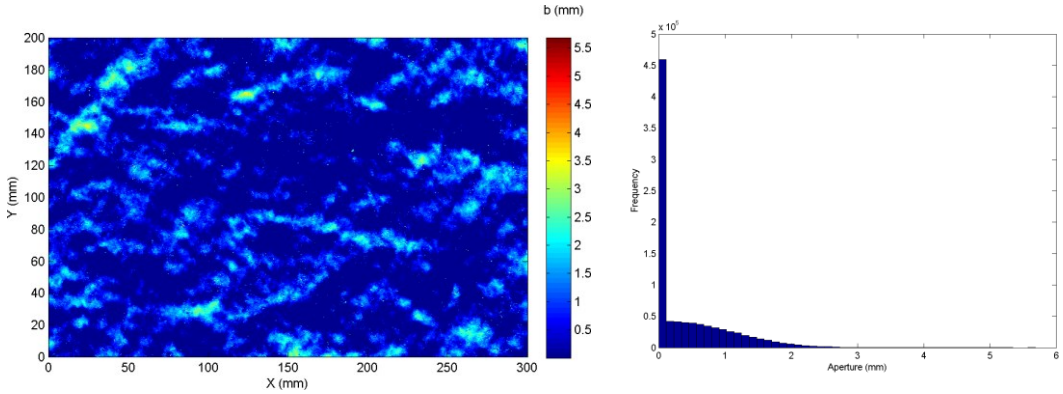

Figure 7: Fracture aperture data for the sheared fracture: large grid case from Ishibashi et al. (2012). The sample was sheared with a 5 mm offset in the y direction. Left: aperture map. Right: histogram of the aperture distribution.

2.2 Shear Fracture

Shear fracture surfaces were generated through compression tests. With the second data set from shear fracture surfaces, the fracture aperture maps were generated with one percent and 40 percent of the total area in contact. These two scenarios represented possible aperture maps for different normal stress conditions. A contact fraction of one percent represented the initial aperture distribution before the application of normal stress. On the other hand, a 40 percent contact area fraction was equivalent to fracture surfaces with applied normal stress. For each percent contact condition, two fracture surface pairing configurations were tested to determine how the addition of a shear offset would change the aperture distribution. The first configuration had the original surfaces paired together (mated configuration) while the second configuration had a 5 mm shear offset in the y direction (sheared configuration).

2.2.1 Shear Fracture: One Percent Contact

Figure 8 and Figure 9 show the original fracture aperture map and histogram for samples 34 and 47, respectively. Both aperture maps have rough surfaces but with no prominent lineations. Because of the small contact area, high aperture values can be observed. For sample 34 (Figure 8), the vertical lineations come from rock breakage. The histogram plots show a Gaussian or normal distribution. Fracture aperture maps and histograms for Samples 48 and 52 are shown in Figure 10 and Figure 11, respectively. Similar to the sandstone samples, the frequency distribution curves are Gaussian. Compared to the sandstone samples, however, the aperture maps for samples 48 and 52 illustrate higher aperture values. The results for the sheared fracture cases with offset are similar to the mated case as shown in Appendix 1. Hence, adding a 5 mm offset in the y direction did not significantly change the frequency distribution characteristics of the fracture aperture.

2.2.2 Shear Fracture: 40 Percent Contact

The 40 percent contact case is similar to the possible aperture distribution after the application of normal stress. Because of the increase in the contact area, the aperture values are lower. Figure 12 shows the aperture map and histogram plot for sample 34. Unlike the one percent contact cases, the frequency distribution is lognormal. Similar to Figure 8, the aperture map shows some lineations of high aperture values. For sample 47, as shown in Figure 13, the frequency distribution is also lognormal. Moreover, there are no prominent lineations in the aperture map. With the granite samples, presented in Figure 14 and Figure 15, the aperture frequency distribution is also lognormal. Sample 52 displays a prominent high aperture feature that is parallel to the x axis. On the other hand, sample 48 does not show a preferential direction of spatial continuity.

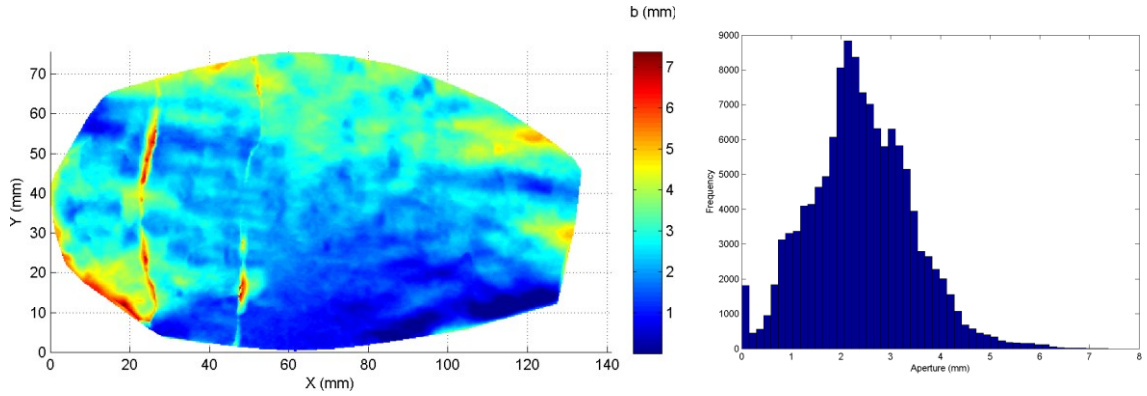

Figure 8: Mated fracture aperture data for sample 34: one percent contact area. Left: aperture map. Right: histogram of the aperture distribution.

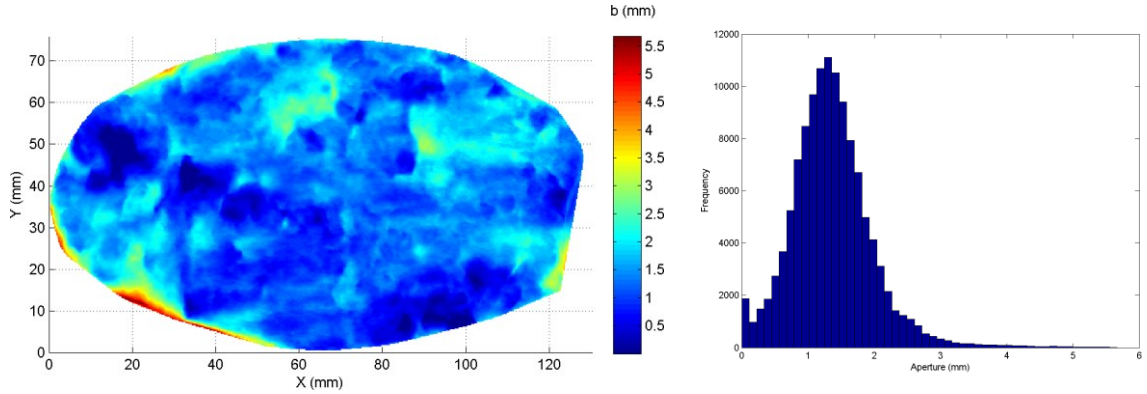

Figure 9: Mated fracture aperture data for sample 47: one percent contact area. Left: aperture map. Right: histogram of the aperture distribution.

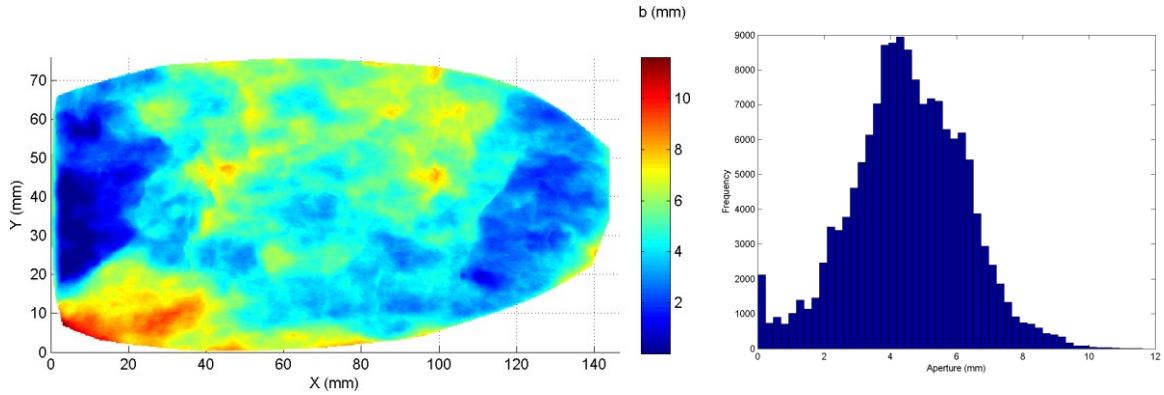

Figure 10: Mated fracture aperture data for sample 48: one percent contact area. Left: aperture map. Right: histogram of the aperture distribution.

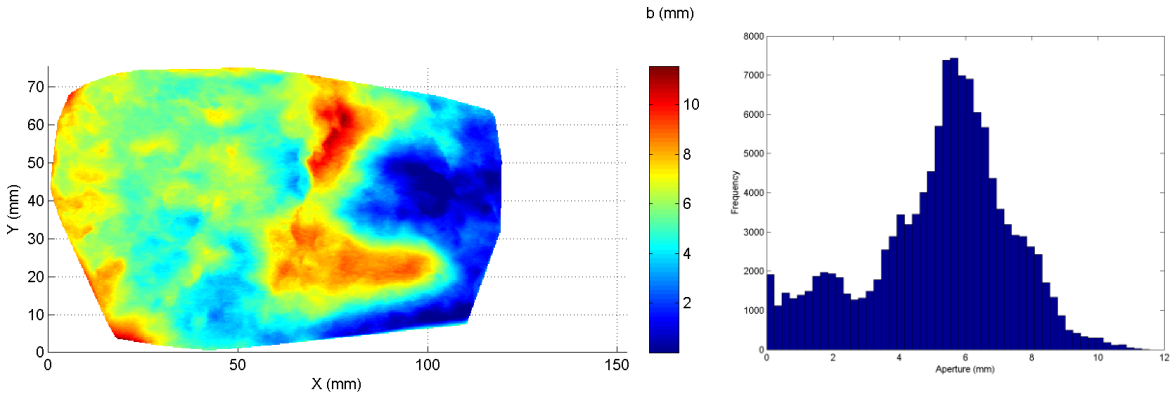

Figure 11: Mated fracture aperture data for sample 52: one percent contact area. Left: aperture map. Right: histogram of the aperture distribution.

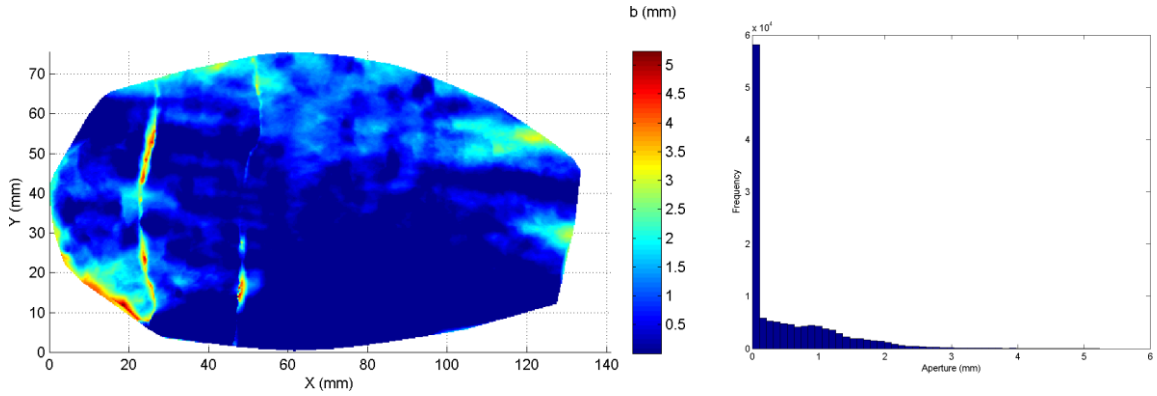

Figure 12: Mated fracture aperture data for sample 34: 40 percent contact. Left: aperture map. Right: histogram of the aperture distribution.

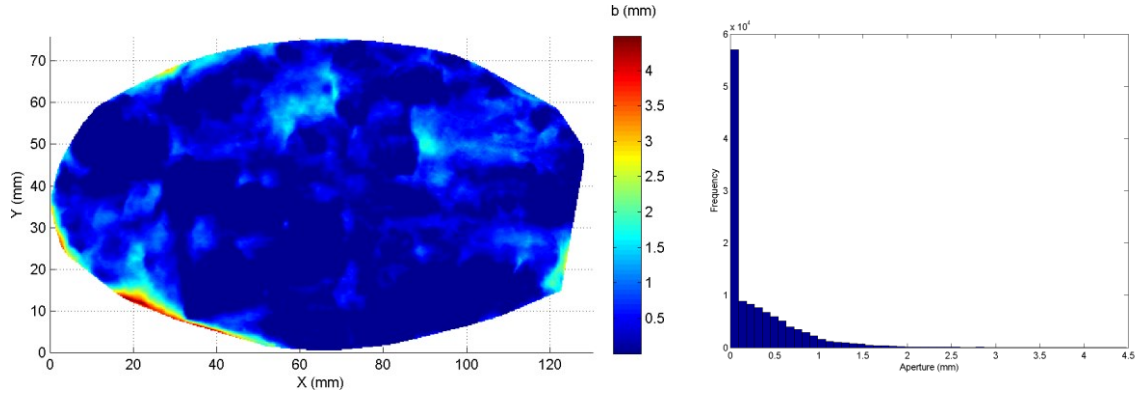

Figure 13: Mated fracture aperture data for sample 47: 40 percent contact. Left: aperture map. Right: histogram of the aperture distribution.

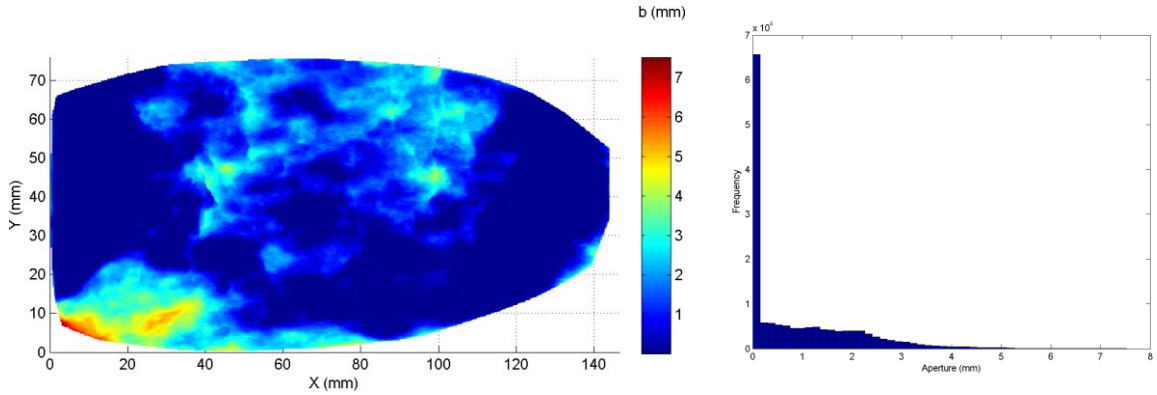

Figure 14: Mated fracture aperture data for sample 48: 40 percent contact. Left: aperture map. Right: histogram of the aperture distribution.

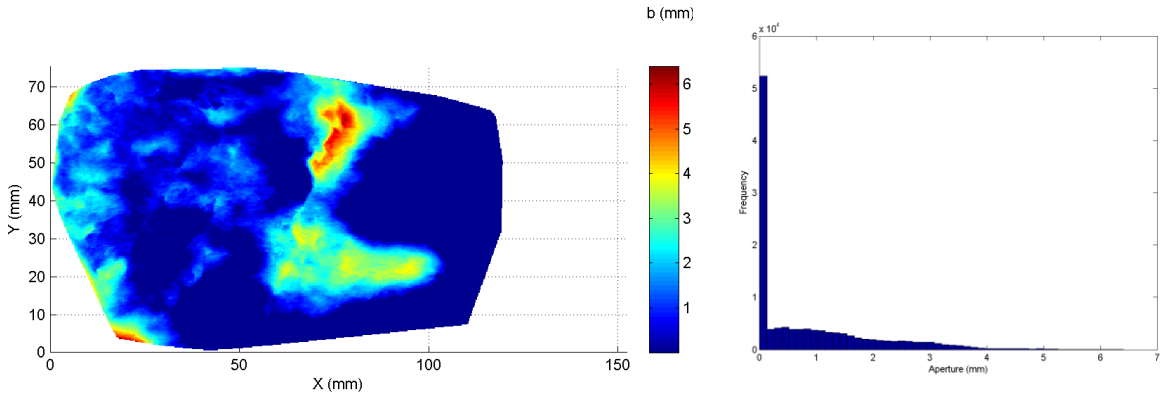

Figure 15: Mated fracture aperture data for sample 52: 40 percent contact. Left: aperture map. Right: histogram of the aperture distribution.

3.VARIOGRAM MODELS

Analysis of the frequency distribution provides some insights on the overall aperture distribution. A lognormal distribution indicates that low aperture values dominate while a Gaussian distribution specifies an even spread of aperture values. However, the frequency distribution is not adequate in describing the spatial distribution of aperture. Moreover, it is hard to identify patterns of spatial continuity through plain visual inspection of the aperture maps. Thus, two-point correlations must be used to quantitatively detect patterns of continuity within the fracture. Trends in the spatial correlation of fracture aperture values can then be related to the generation mechanism. For instance, the orientation with the highest spatial correlation may be consistent with the direction of shear. Moreover, trends in spatial correlation can indicate the existence of channels in the aperture distribution which could result to flow channeling.

The semivariogram or variogram describes the spatial autocorrelation using the variance of the difference in the values of two points separated by a lag distance h in a specific direction. Because it is based on the correlation of two points, it does not fully capture the spatial relationships within the fracture. Still, the variogram can be used to quantify the general features of the fracture aperture distribution in space. Equation 1 shows the general expressions for the semivariogram in terms of the expected value and the variance (Hohn, 1999).

$$\begin{aligned}\gamma^*(h) &= E\{[Z(u_\alpha) - Z(u_\alpha + h)]^2\} \\ &= Var\{Z(u_\alpha) - Z(u_\alpha + h)\} \\ &= \frac{1}{2n_p}\sum_{i=1}^{n_p}[Z(u_\alpha) - Z(u_\alpha + h)]^2\end{aligned} \tag{1}$$

where γ^*, h, n_p, Z, u_α are variogram, lag distance, number of points, variable value, and location, respectively.

Sample pairs that are located near each other (small h) have similar values and small semivariogram values. On the other hand, as the distance h increases, the autocorrelation decreases and the semivariogram approaches the simple variance. This limiting value is also called the sill (C_s) and the minimum lag distance needed to reach the sill is called the range (a). In order to describe the semivariogram behavior with respect to the lag distance, the important parameters are the behavior at low lag distance values and the presence of a sill or boundedness (Hohn, 1999). These parameters are identified from interpretations on the geology. The five commonly used theoretical semivariogram models are the nugget effect, spherical, exponential, Gaussian, and power models (Goovaerts, 1997) as shown in the following equations.

$$\begin{aligned}\gamma^*(h) &= 0 \quad h = 0 \\ &= C_s \quad h > 0\end{aligned} \tag{2}$$

$$\begin{aligned}\gamma^*(h) &= C_s\left[\frac{3}{2}\left(\frac{h}{a}\right) - \frac{1}{2}\left(\frac{h}{a}\right)^3\right] \quad h < a \\ &= C_s \quad h \geq a\end{aligned} \tag{3}$$

$$\gamma^*(h) = C_s\left[1 - e^{\left(-\frac{3h}{a}\right)}\right] \tag{4}$$

$$\gamma^*(h) = C_s\left[1 - e^{\left(-\frac{3h^2}{a^2}\right)}\right] \tag{5}$$

$$\gamma^*(h) = C_s h^\omega, 0 < \omega < 2 \tag{6}$$

where a, C_s, ω are the correlation range, sill and fractal constant, respectively.

The nugget effect model is discontinuous at the origin as shown in Equation 2. This effect can be attributed to measurement errors, sparse data, and insufficient sampling. For the spherical model (Equation 3), the behavior at the origin is linear. The sill is reached when $h = \frac{2}{3}a$. Similar to the spherical model, the exponential model (Equation 4) behaves linearly at the origin. However, only 95 percent of the sill is reached at the practical range a. Comparing the exponential and spherical models, the exponential model changes more rapidly at smaller lag distance values but it is smoother at the transition range near the sill. Another bounded model is the Gaussian model shown in Equation 5. The exponential and Gaussian models approach the sill asymptotically beyond a (Goovaerts, 1997). Unlike the exponential and spherical models, however, the Gaussian model has a parabolic behavior at the origin. Because of its smoothness, the Gaussian model cannot be used for data sets that have noise. The fifth model, called the power model, is unbounded and it is related to fractals. Its behavior at the origin depends on the value of ω as shown in Equation 6. The behavior is approximately linear for $\omega \leq 1$ and parabolic for $\omega > 1$ (Goovaerts, 1997).

The five theoretical models can be combined to form more realistic nested variogram models by adding them as shown in the equation below.

$$\gamma^*(h) = \gamma_1^*(h) + \gamma_2^*(h) + \cdots + \gamma_n^*(h) \tag{7}$$

where $\gamma_1^*(h), \gamma_2^*(h), \gamma_n^*(h)$ are structure 1, structure 2, and structure n, respectively.

In addition, the semivariogram model can be calculated at different orientations. A geometric anisotropy exists when the semivariogram at different orientations have the same sill but different range values. The rose diagram plot of the range at different orientations or azimuth will be an ellipse (Goovaerts, 1997). Thus, geometric anisotropy can possibly be used to infer the direction of relative motion and stress conditions. On the other hand, zonal anisotropy is described as the situation when the sill values vary

with the direction. In terms of variogram modeling, zonal anisotropy can be defined by specifying a large range value in the direction perpendicular to the higher sill direction.

Figure 16 shows an example of the experimental variogram values and the best fit model for the mated wedge fracture with the large grid. Comparing the variogram plots for the x direction (0° from the x axis) and y direction (90° from the x axis), it can be observed that both have the same sill value of 0.05. Additionally, both have the same range value of 5 mm which indicates that there is no preferential direction for spatial continuity. Moreover, the variogram value changes rapidly at small lag distance values in a behavior consistent with the exponential model.

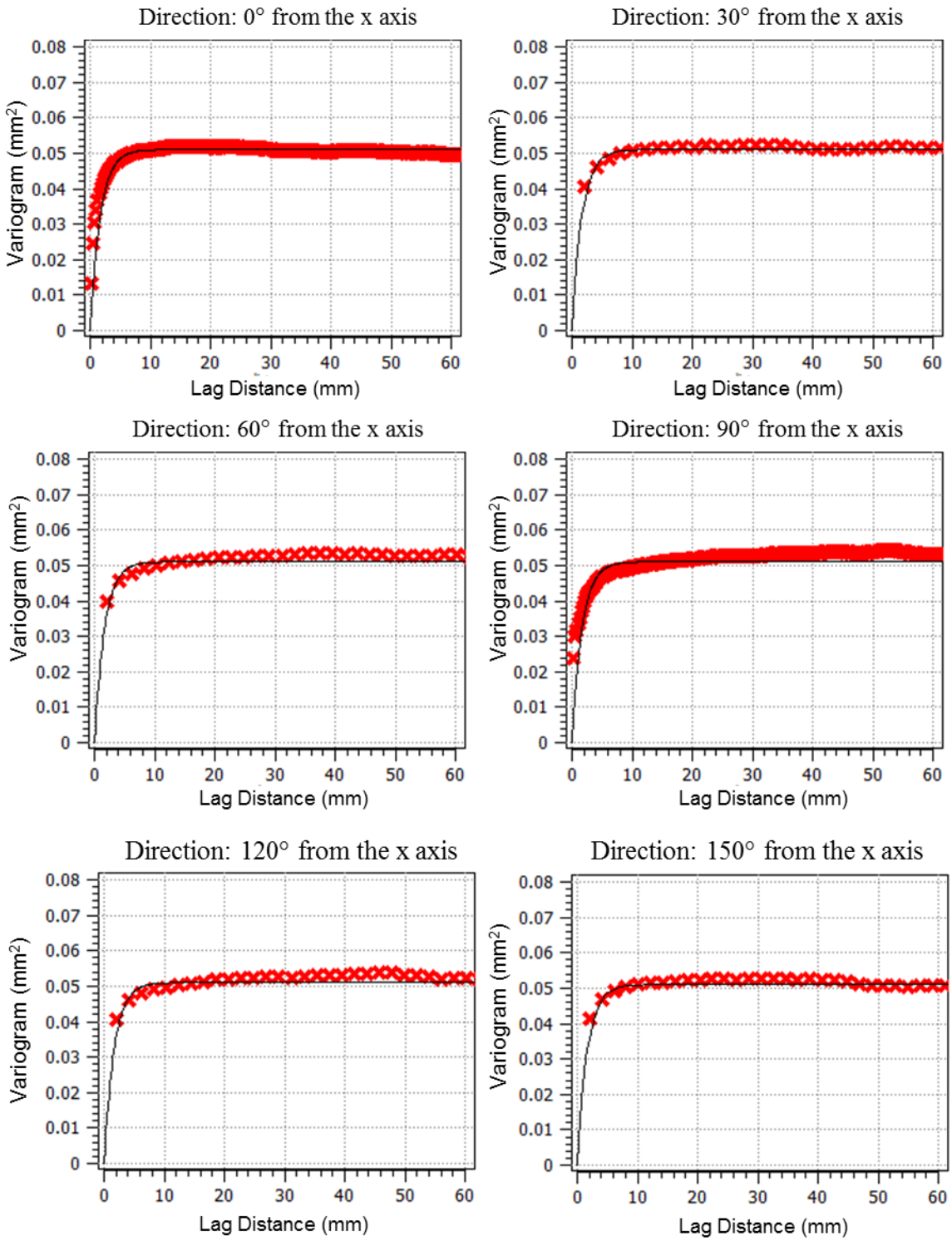

Figure 16: Sample experimental variograms (red markers) and best fit model (solid line) for the mated: large grid case in directions 0°, 30°, 60°, 90°, 120°, 150° from the x axis.

4. RESULTS AND DISCUSSION

The variogram models for all the other fracture aperture maps were determined in a manner similar to the one used to generate Figure 16. To determine the appropriate variogram model, the following characteristics of the experimental variogram were matched: ranges in the x and y directions, sill value, and variogram behavior at low lag distance values. In addition, the best fit model must be consistent with the experimental variogram plots at different orientations. Trends in the variogram models are correlated with the generation mechanisms in terms of the fracture surface creation methods, fracture surface pairing configurations, and the shear direction.

4.1 Wedge Fracture

For the wedge fractures, mated and sheared fracture surface pairings were compared. In addition, the direction of shear offset was compared to the orientation of the maximum range. Table 1 shows the variogram models for the mated and sheared scenarios for the small grid wedge fracture. The mated small grid case had one structure while the sheared case had two structures. Comparing the first structure with an exponential model, the mated case exhibited no geometric anisotropy while the sheared case had a longer correlation range in the 90° azimuthal direction (x direction). Thus, the sheared case variogram model showed a preferential direction perpendicular to the direction of the shear displacement. Additionally, the sheared case variogram exhibited zonal anisotropy that was modelled using the second exponential structure. A higher sill value was observed in the x direction which indicates a greater variety of aperture values in this orientation.

Similar mated versus sheared characteristics were documented in the variogram models for the medium and large grid cases as presented in Table 2 and Table 3, respectively. Table 2 has two structures while Table 3 has one structure. For both medium and large grid cases, the mated fracture variogram was isotropic while the sheared fracture variogram model was anisotropic with a greater correlation in the x direction. The degree of geometric anisotropy can be approximated by the ratio of the maximum and medium range values in the dominant orientation. In the three grid cases of wedge fractures, the medium grid case showed the highest degree of anisotropy with a minimum and maximum range of 38 mm and 13 mm, respectively. These observations were consistent with the channels found in the aperture maps. Hence, the variogram models could be used to identify the existence of channels and quantitatively describe the extent of these channels. Another advantage of using variogram models is for generating fracture aperture maps with the same spatial characteristics.

Table 1: Variogram model comparison of mated versus sheared fractures for the small grid case from Ishibashi et al. (2012). The azimuth is the angle from the y axis. The maximum range shows the correlation length in the direction of the azimuth.

	Mated	Sheared
Structure 1 Contribution (Exponential):	0.0065	0.08
Maximum Range (mm):	5	27
Medium Range (mm):	5	12
Azimuth (^{o}):	90	90
Structure 2 Contribution (Exponential):		0.015
Maximum Range (mm):		10000
Medium Range (mm):		30
Azimuth (^{o}):		0

Table 2: Variogram model comparison of mated versus sheared fractures for the medium grid case from Ishibashi et al. (2012). The azimuth is the angle from the y axis. The maximum range shows the correlation length in the direction of the azimuth.

	Mated	Sheared
Structure 1 Contribution (Exponential):	0.055	0.5
Maximum Range (mm):	7	38
Medium Range (mm):	7	13
Azimuth (^{o}):	90	90
Structure 2 Contribution (Spherical):		0.05
Maximum Range (mm):		10000
Medium Range (mm):		20
Azimuth (^{o}):		90

Table 3: Variogram model comparison of mated versus sheared fractures for the large grid case from Ishibashi et al. (2012). The azimuth is the angle from the y axis. The maximum range shows the correlation length in the direction of the azimuth.

	Mated	Sheared
Structure 1 Contribution (Exponential):	0.051	0.34
Maximum Range (mm):	5	25
Medium Range (mm):	5	13
Azimuth (^{o}):	90	90

4.2 Shear Fracture

Compressions tests were used to generate shear fracture surfaces. Therefore, shear fracture surfaces were expected to have aperture distribution characteristics indicative of the shearing process. Two contact area fraction scenarios were created to represent different stages in typical shear box experiments. The initial aperture distribution was approximated with a one percent contact area fraction. On the other hand, the aperture distribution after the application of normal stress was represented by a 40 percent contact area fraction. In addition, the effect of a 5 mm shear offset for each contact area fraction case was investigated. The mated surface pairing configuration was compared to the sheared surface pairing configuration which had a 5mm shear offset in the y direction.

4.2.1 Shear Fracture: One Percent Contact

The best fit variogram models for the sandstone samples, samples 34 and 47, are shown in Table 4 and Table 5, respectively. Comparisons were made for the mated and sheared configuration cases. Both samples showed geometric anisotropy for the mated and sheared configuration cases, as indicated by structure 1. Additionally, the geometric anisotropy for the sheared configuration cases exhibited a stronger correlation in the x direction which is perpendicular to the direction of the shear offset. However, sample 47 had a slightly higher degree of anisotropy compared to sample 34. Moreover, the sheared configuration case for sample 47 had a higher degree of anisotropy than the corresponding mated configuration case. Similarly, the sheared configuration case for sample 34 also had a higher degree of anisotropy compared to the mated configuration case. Another similarity between the two samples was the characteristic of zonal anisotropy. Samples 34 and 47 had a higher sill value in the y direction.

The results for the granite samples, samples 48 and 52, are shown in Table 6 and Table 7. Similar to the sandstone samples, the variogram model structure types for the mated and sheared configuration cases were identical. Sample 48 exhibited significant geometric anisotropy for the sheared configuration case but not for the mated configuration case. Moreover, the mated configuration case for sample 48 was slightly more continuous in the y direction. The deviation in the preferential direction of the mated configuration case for sample 48 was attributed to surface degradation or gouge formation which could even out the surface elevations. On the other hand, sample 52 showed significant geometric anisotropy for both mated and sheared configuration cases. For both samples, the sheared configuration cases were more continuous in the x direction which was perpendicular to the direction of the shear offset. In terms of zonal anisotropy, sample 48 had a higher sill value in the y direction while sample 52 has a higher sill value in the x direction.

Table 4: Variogram model comparison of mated versus sheared surface pairing configurations for sample 34 with one percent contact. The sheared configuration has a 5 mm offset in the y direction. The azimuth is the angle from the y axis. The maximum range shows the correlation length in the direction of the azimuth.

	Mated	Sheared
Structure 1 Contribution (Exponential):	0.5	1
Maximum Range (mm):	28	45
Medium Range (mm):	23	25
Azimuth (^{o}):	90	90
Structure 2 Contribution (Exponential):	0.18	0.8
Maximum Range (mm):	10000	10000
Medium Range (mm):	23	40
Azimuth (^{o}):	90	90

Table 5: Variogram model comparison of mated versus sheared surface pairing configurations for sample 47 with one percent contact. The sheared configuration has a 5 mm offset in the y direction. The azimuth is the angle from the y axis. The maximum range shows the correlation length in the direction of the azimuth.

	Mated	Sheared
Structure 1 Contribution (Exponential):	0.2	0.45
Maximum Range (mm):	24	47
Medium Range (mm):	18	25
Azimuth (^{o}):	90	90
Structure 2 Contribution (Exponential):	0.2	0.1
Maximum Range (mm):	10000	10000
Medium Range (mm):	20	25
Azimuth (^{o}):	120	90

Table 6: Variogram model comparison of mated versus sheared surface pairing configurations for sample 48 with one percent contact. The sheared configuration has a 5 mm offset in the y direction. The azimuth is the angle from the y axis. The maximum range shows the correlation length in the direction of the azimuth.

	Mated	Sheared
Structure 1 Contribution (Spherical):	2.5	2.5
Maximum Range (mm):	42	41
Medium Range (mm):	40	30
Azimuth (^{o}):	0	90
Structure 2 Contribution (Spherical):	1	1
Maximum Range (mm):	10000	10000
Medium Range (mm):	60	40
Azimuth (^{o}):	90	90

Table 7: Variogram model comparison of mated versus sheared surface pairing configurations for sample 52 with one percent contact. The sheared configuration has a 5 mm offset in the y direction. The azimuth is the angle from the y axis. The maximum range shows the correlation length in the direction of the azimuth.

	Mated	Sheared
Structure 1 Contribution (Spherical):	3.4	3
Maximum Range (mm):	42	45
Medium Range (mm):	21	20
Azimuth (^{o}):	90	90
Structure 2 Contribution (Spherical):	2	2.2
Maximum Range (mm):	10000	10000
Medium Range (mm):	50	40
Azimuth (^{o}):	0	0

4.2.2 Shear Fracture: 40 Percent Contact

The 40 percent contact case represents the aperture distribution with applied normal stress. Consistent with the one percent case, the effect of an additional 5 mm offset in the y direction was evaluated. Table 8 and Table 9 show the best fit variogram models for samples 34 and 47, respectively. Consistent with the one percent case, both samples show geometric anisotropy with a strong correlation in the direction perpendicular to the shear offset for the mated and sheared configuration cases. However, the values for the degree of geometric anisotropy were higher for the 40 percent contact area cases as compared to the one percent contact cases. This observation was consistent with the higher channeling observed in the fracture aperture maps for the 40 percent contact cases. Additionally, in contrast with the one percent case, both samples exhibited no zonal anisotropy. Thus, both samples can be modeled with a single structure in the variogram model.

For sample 48, the mated and sheared configuration cases with a 40 percent contact area fraction had similar variogram models to the corresponding case with one percent contact, as shown in Table 10. The orientation of first structure was consistent with the one percent contact case. However, the degree of geometric anisotropy was higher for the 40 percent contact case. Furthermore, the zonal anisotropy for the one percent contact case was slightly higher compared to the 40 percent case, which meant that there was a higher degree of variety in aperture values for the one percent contact case of sample 48. Consistent with the variogram model for the one percent case, sample 52 exhibited a higher spatial correlation for the x direction as shown in Table 11. Moreover, the sheared configuration case showed a slight increase in the degree of geometric anisotropy compared to the mated configuration case. Furthermore, the 40 percent contact case of sample 52 had zonal isolation consistent with the one percent case.

Table 8: Variogram model comparison of mated versus sheared surface pairing configurations for sample 34 with 40 percent contact. The sheared configuration has a 5 mm offset in the y direction. The azimuth is the angle from the y axis. The maximum range shows the correlation length in the direction of the azimuth.

	Mated	Sheared
Structure 1 Contribution (Exponential):	0.5	0.9
Maximum Range (mm):	55	60
Medium Range (mm):	24	30
Azimuth (^{o}):	90	90

Table 9: Variogram model comparison of mated versus sheared surface pairing configurations for sample 47 with 40 percent contact. The sheared configuration has a 5 mm offset in the y direction. The azimuth is the angle from the y axis. The maximum range shows the correlation length in the direction of the azimuth.

	Mated	Sheared
Structure 1 Contribution (Exponential):	0.21	0.2
Maximum Range (mm):	30	40
Medium Range (mm):	20	20
Azimuth (^{o}):	90	90

Table 10: Variogram model comparison of mated versus sheared surface pairing configurations for sample 48 with 40 percent contact. The sheared configuration has a 5 mm offset in the y direction. The azimuth is the angle from the y axis. The maximum range shows the correlation length in the direction of the azimuth.

	Mated	Sheared
Structure 1 Contribution (Spherical):	1	1.1
Maximum Range (mm):	67	42
Medium Range (mm):	36	25
Azimuth (^{o}):	0	90
Structure 2 Contribution (Spherical):	1	0.4
Maximum Range (mm):	10000	10000
Medium Range (mm):	60	40
Azimuth (^{o}):	90	90

Table 11: Variogram model comparison of mated versus sheared surface pairing configurations for sample 52 with 40 percent contact. The sheared configuration has a 5 mm offset in the y direction. The azimuth is the angle from the y axis. The maximum range shows the correlation length in the direction of the azimuth.

	Mated	Sheared
Structure 1 Contribution (Spherical):	1	1
Maximum Range (mm):	40	40
Medium Range (mm):	18	17
Azimuth (^{o}):	90	90
Structure 2 Contribution (Spherical):	0.8	0.6
Maximum Range (mm):	10000	10000
Medium Range (mm):	30	20
Azimuth (^{o}):	0	0

In summary, all of the shear fracture samples with a sheared surface pairing configuration exhibited spatial continuity in the direction perpendicular to the direction of the shear offset. Furthermore, the mated and sheared surface pairing configuration cases had consistent variogram model structure types. Moreover, an increase the area of contact resulted to an increase in the degree of geometric anisotropy for most fracture cases. Comparing the sandstone and granite shear fractures, it was observed that the sandstone shear fractures all had exponential variogram models while the granite shear fractures had spherical models. This variogram model difference could be due to difference in the rock failure behavior of the two rock types. However, more samples would be needed to verify this observation.

The main difference between the fracture surfaces created with a wedge and the surfaces created in shear experiments was the effect of the additional shear offset. Unlike the wedge fracture cases, the variogram models for most of the shear fracture cases exhibited preferential directions even for the mated configuration cases which had no shear offset. This observation could be attributed to the creation of lineations during the original shearing process that created the initial shear fracture surfaces prior to the addition of a shear offset. Thus, the variogram for the direct mated pairing of the two surfaces can provide an indication of the original fracture surface generation mechanism.

5. CONCLUSIONS AND FUTURE WORK

Rough fracture surfaces can lead to permeability distributions that demonstrate flow channeling effects. In geothermal reservoirs, flow channeling within the fracture can also reduce the surface area available for heat conduction. Characterization parameters describing the spatial distribution of fracture aperture can be correlated with flow channeling. In addition, characterization parameters can be used to infer the generation mechanisms of rough fracture creation. The variogram can be used to infer two-point correlations in space. Experimental variogram plots can be modeled using standard variogram models. The orientation of highest spatial continuity is determined based on the direction with the highest range value.

In the presence of additional shear offset, wedge fracture surfaces generated artificially and shear fracture surfaces generated by compression tests both exhibit strong channeling in the direction perpendicular to the direction of the shear offset. For wedge fractures, adding a shear offset significantly increased the degree of channeling in the aperture distribution. Mated wedge fractures exhibited no preferential directions while sheared wedge fractures showed higher spatial continuity. On the other hand, results from shear fracture surfaces from compression tests showed that the additional shear offset did not consistently increase the degree of geometric anisotropy of the corresponding mated fractures. Furthermore, in comparing the wedge and shear fractures, the mated shear fractures displayed geometric anisotropy while the mated wedge fractures did not. Hence, the difference between fracture surface generation mechanisms could be identified using the variogram models.

Having identified the potential of variogram model parameters for capturing general trends of spatial continuity, the next stage of this study will focus on correlating variogram parameters to flow channeling and heat transport effects. Future work will include flow simulations and application of geostatistical techniques to generate permeability maps with similar variogram models.

ACKNOWLEDGEMENTS

The authors would like to thank David Pollard for providing the shear fracture data set. Elevation measurements for this data set were made by Rebecca Strickfaden on core samples fractured in compression tests performed by Dave Lockner at the USGS in

Menlo Park, CA. In addition, the authors also thank Noriaki Watanabe and Takuya Ishibashi for providing the wedge fracture aperture data.

REFERENCES

Gale, J. E.: Comparison of Coupled Fracture Deformation and Fluid Flow Models with Direct Measurements of Fracture Pore Structure and Stress-flow Properties. *The 28th US Symposium on Rock Mechanics (USRMS)*, (1987).

Goovaerts, P.: Geostatistics for Natural Resources Evaluation, *Oxford University Press*, (1997).

Hakami, E. and Larsson, E.: Aperture Measurements and Flow Experiments on a Single Natural Fracture, *International Journal of Rock Mechanics and Mining Sciences & Geomechanics Abstracts*, **33(4)**, (1996), 395-404.

Hohn, M. E.: Geostatistics and Petroleum Geology, *Springer*, (1999).

Isaaks, E. H. and Srivastava, R. M.: Applied Geostatistics, *Oxford University Press*, (1989).

Ishibashi, T., Watanabe, N., Hirano, N., Okamoto, A., and Tsuchiya, N.: Upgrading of Aperture Model based on Surface Geometry of Natural Fracture for Evaluating Channeling Flow, *GRC Transactions*, **36**, (2012), 481-486.

Iwano, M. and Einstein, H. H.: Stochastic Analysis of Surface Roughness, Aperture and Flow in a Single Fracture. *ISRM International Symposium-EUROCK 93*, (1993).

Klinkenberg, B.: A Review of Methods used to Determine the Fractal Dimension of Linear Features, *Mathematical Geology*, **26(1)**, (1994), 23-46.

Lee, H. and Cho, T.: Hydraulic Characteristics of Rough Fractures in Linear Flow under Normal and Shear Load, *Rock Mechanics and Rock Engineering*, **35(4)**, (2002), 299-318.

Pyrak-Nolte, L. J., Montemagno, C. D., and Nolte, D. D.: Volumetric Imaging of Aperture Distributions in Connected Fracture Networks, *Geophysical Research Letters*, **24(18)**, (1997), 2343-2346.

Remy, N., Boucher, A., and Wu, J.: Applied Geostatistics with SGeMS: a User's Guide, *Cambridge University Press*, (2009).

Renshaw, C. E.: On the Relationship between Mechanical and Hydraulic Apertures in Rough-walled Fractures, *Journal of Geophysical Research*, **100(B12)**, (1995).

Sausse, J.: Hydromechanical Properties and Alteration of Natural Fracture Surfaces in the Soultz Granite, *Tectonophysics*, **348(1)**, (2002), 169-185.

Watanabe, N., Hirano, N., and Tsuchiya, N.: Determination of Aperture Structure and Fluid Flow in a Rock Fracture by High-resolution Numerical Modeling on the Basis of a Flow-through Experiment under Confining Pressure, *Water Resources Research*,**44(6)**, (2008).

Watanabe, N., Hirano, N., and Tsuchiya, N.: Diversity of Channeling Flow in Heterogeneous Aperture Distribution Inferred from Integrated Experimental-Numerical Analysis on Flow through Shear Fracture in Granite, *Journal of Geophysical Research: Solid Earth (1978-2012)*, **114(B4)**, (2009).

APPENDICES

A.1. Shear Fractures with a One Percent Contact Area Fraction: Sheared Surface Pairing Configuration

This section shows the aperture maps and histogram plots for the shear fracture samples with additional shear offset and a one percent contact area fraction. The fractures are created by adding a 5 mm offset in the y direction. Results for samples 34, 47, 48, and 52 are shown in Figure 17, Figure 18, Figure 19, and Figure 20.

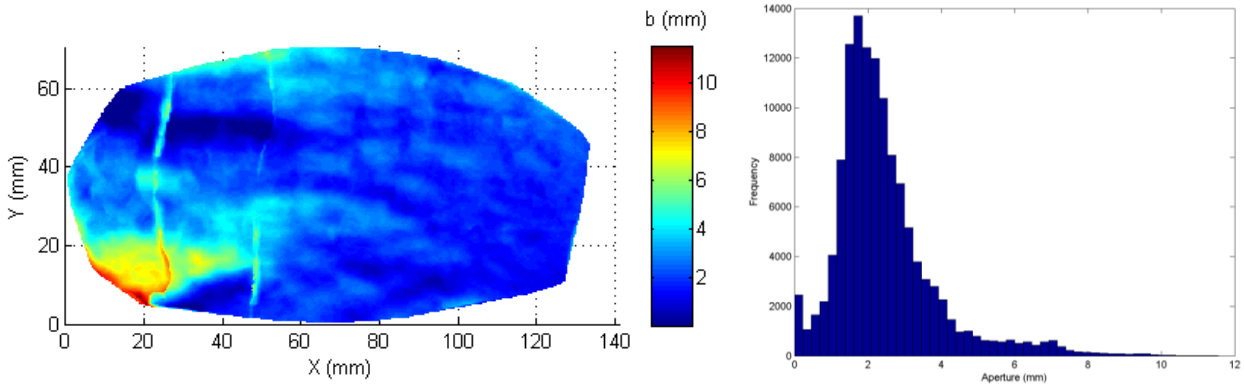

Figure 17: Sheared fracture aperture data for sample 34 with a 5 mm offset in the y direction: one percent contact area. Left: aperture map. Right: histogram of the aperture distribution.

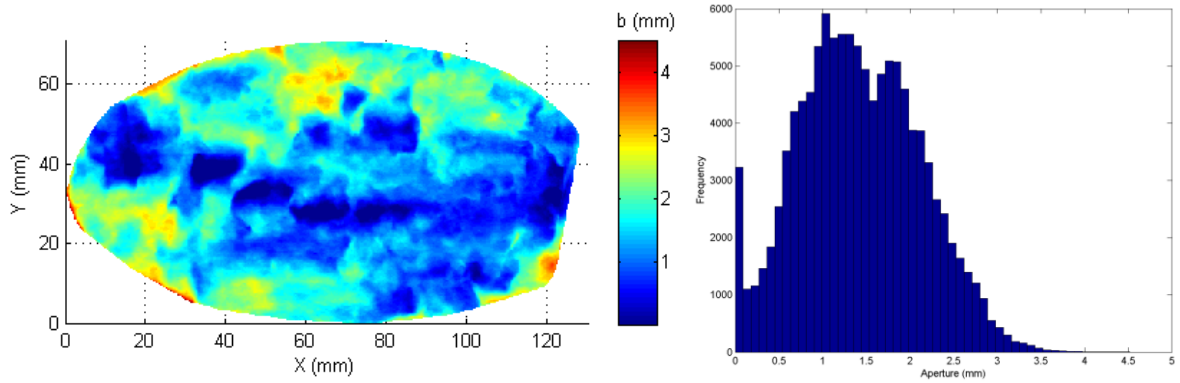

Figure 18: Sheared fracture aperture data for sample 47 with a 5 mm offset in the y direction: one percent contact area. Left: aperture map. Right: histogram of the aperture distribution.

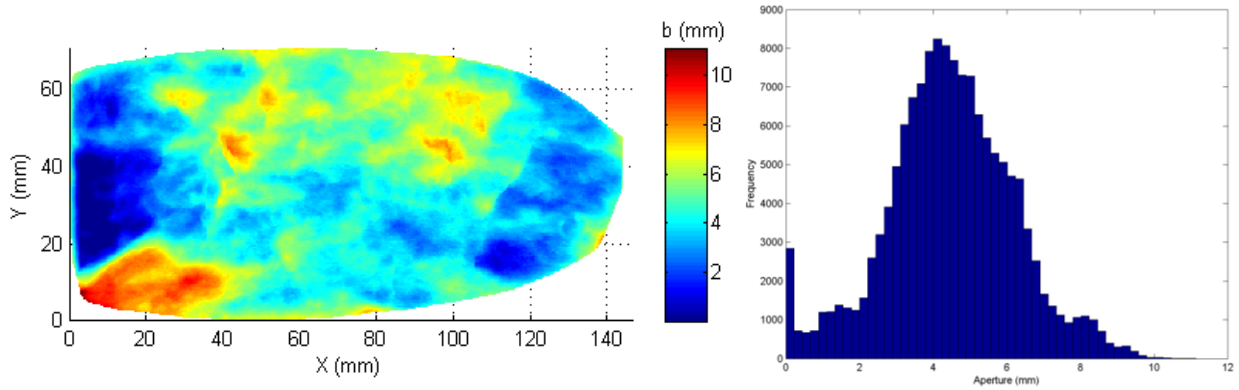

Figure 19: Sheared fracture aperture data for sample 48 with a 5 mm offset in the y direction: one percent contact area. Left: aperture map. Right: histogram of the aperture distribution.

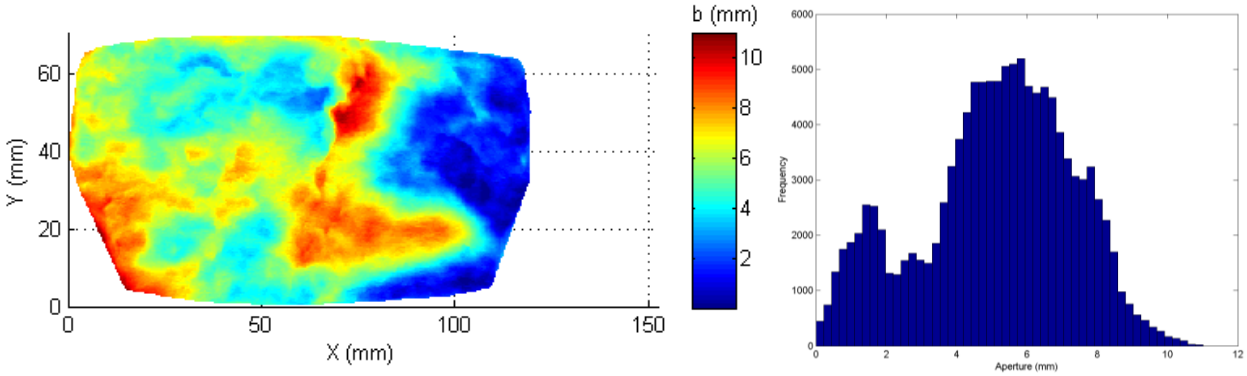

Figure 20: Sheared fracture aperture data for sample 52 with a 5 mm offset in the y direction: one percent contact area. Left: aperture map. Right: histogram of the aperture distribution.

A.2. Shear Fractures with a 40 Percent Contact Area Fraction: Sheared Surface Pairing Configuration

Aperture maps and histogram plots for the shear fracture case with additional shear offset and a 40 percent contact area fraction are shown from Figure 21 to Figure 24. The results for samples 34, 47, 48, and 52, are presented in Figure 21, Figure 22, Figure 23, and Figure 24, respectively.

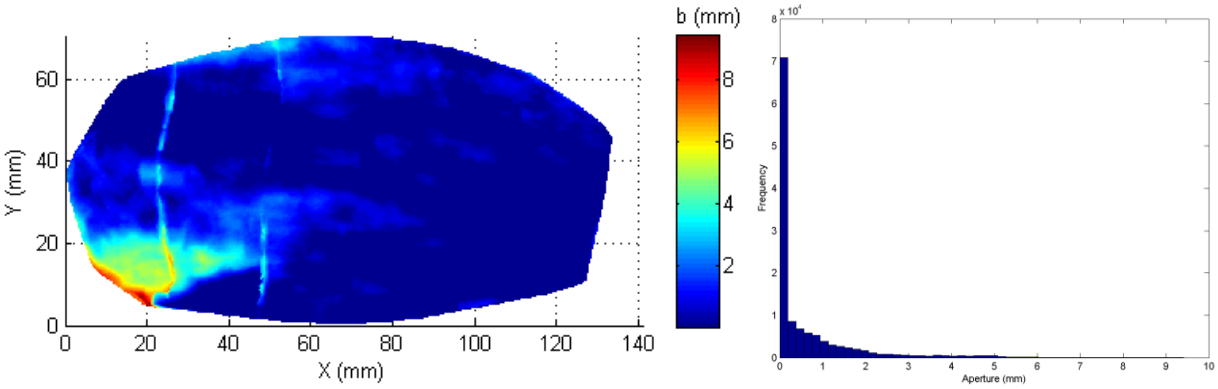

Figure 21: Sheared fracture aperture data for sample 34 with a 5 mm offset in the y direction: 40 percent contact. Left: aperture map. Right: histogram of the aperture distribution.

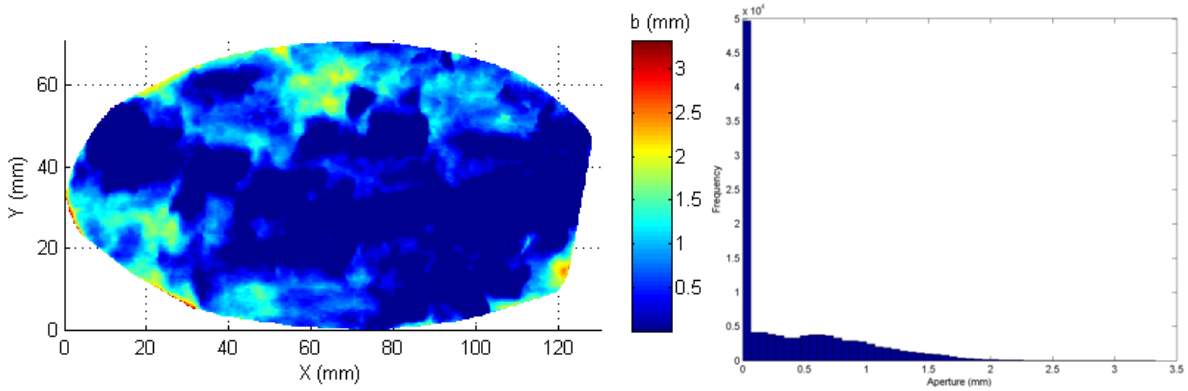

Figure 22: Sheared fracture aperture data for sample 47 with a 5 mm offset in the y direction: 40 percent contact. Left: aperture map. Right: histogram of the aperture distribution.

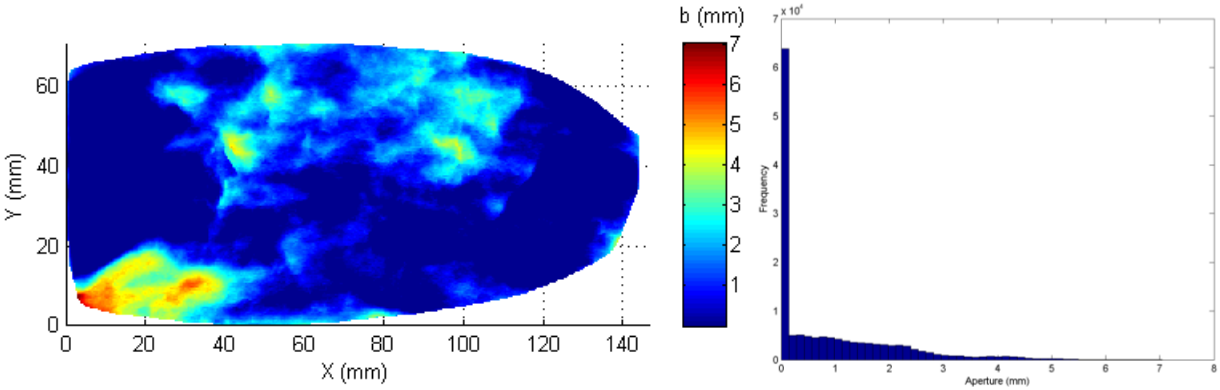

Figure 23: Sheared fracture aperture data for sample 48 with a 5 mm offset in the y direction: 40 percent contact. Left: aperture map. Right: histogram of the aperture distribution.

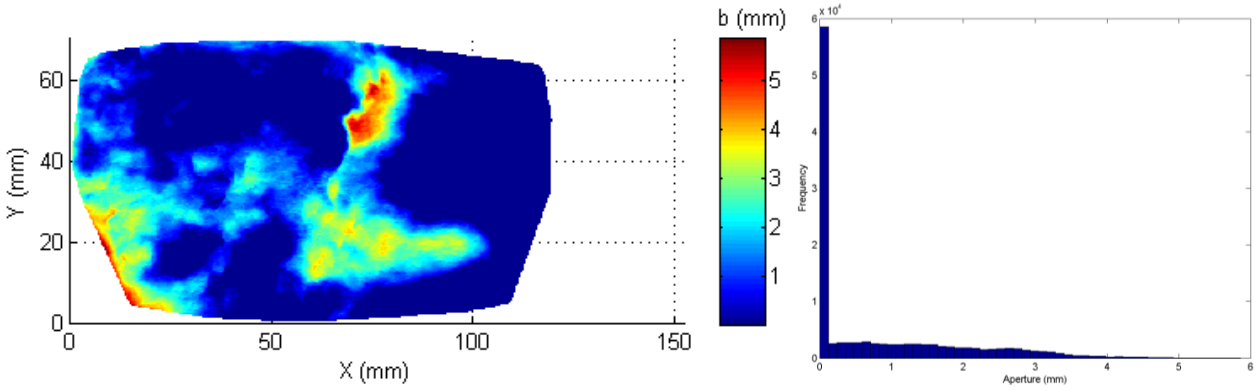

Figure 24: Sheared fracture aperture data for sample 52 with a 5 mm offset in the y direction: 40 percent contact. Left: aperture map. Right: histogram of the aperture distribution.